

**Aboveground biomass corresponds strongly with drone-derived canopy height but weakly with greenness (NDVI) in a shrub tundra landscape**

**Contributors**

Andrew M. Cunliffe<sup>1\*</sup>, Jakob Assmann<sup>2</sup>, Gergana Daskalova<sup>3</sup>, Jeff Kerby<sup>4</sup>, Isla H. Myers-Smith<sup>3</sup>

**Affiliations**

<sup>1</sup> Department of Geography, University of Exeter, UK

<sup>2</sup> Department of Bioscience, Aarhus University, DK

<sup>3</sup> School of Geosciences, University of Edinburgh, UK

<sup>4</sup> Aarhus Institute of Advances Studies (AIAS), Aarhus University, DK

\* Corresponding author ([a.cunliffe@exeter.ac.uk](mailto:a.cunliffe@exeter.ac.uk))

**ORCID**

AMC: 0000-0002-8346-4278; IHM-S: 0000-0002-8417-6112; JA: 0000-0002-3492-8419; GD: 0000-0002-5674-5322; JK: 0000-0002-2739-9096

**Keywords**

Vegetation Change; Aboveground Biomass; Vegetation greenness; Normalized Difference Vegetation Index (NDVI); Drones; Arctic Tundra Ecosystems; Structure-from-Motion Photogrammetry

## **Abstract**

Arctic landscapes are changing rapidly in response to warming, but future predictions are hindered by difficulties in scaling ecological relationships from plots to biomes. Unmanned aerial systems (UAS, hereafter 'drones') are increasingly used to observe Arctic ecosystems over broader extents than can be measured using ground-based approaches and facilitate the interpretation of coarse-grained remotely-sensed datasets. However, more information is needed about how drone-acquired remote sensing observations correspond with ecosystem attributes such as aboveground biomass. Working across a willow shrub-dominated alluvial fan at a focal study site in the Canadian Arctic, we conducted peak season drone surveys with a RGB camera and multispectral multi camera array to derive photogrammetric reconstructions of canopy and normalised difference vegetation index (NDVI) maps along with *in situ* point intercept measurements and biomass harvests from 36, 0.25 m<sup>2</sup> plots. We found high correspondence between canopy height measured using *in situ* point intercept compared to drone-photogrammetry (concordance correlation coefficient = 0.808), although the photogrammetry heights were positively biased by 0.14 m relative to point intercept heights. Canopy height was strongly and linearly related to aboveground biomass, with similar coefficients of determination for point framing ( $R^2 = 0.92$ ) and drone-based methods ( $R^2 = 0.90$ ). NDVI was positively related to aboveground biomass, phytomass and leaf biomass. However, NDVI only explained a small proportion of the variance in biomass ( $R^2$  between 0.14 and 0.23 for logged total biomass) and we found moss cover influenced the NDVI-phytomass relationship. Biomass is challenging to infer from drone-derived NDVI, particularly in ecosystems where bryophytes cover a large proportion of the land surface. Our findings suggest caution with broadly attributing change in fine-grained NDVI to biomass differences across biologically and topographically complex tundra landscapes. By comparing structural, spectral and on-the-ground ecological measurements, we can improve understanding of tundra vegetation change as inferred from remote sensing.

## 1. Introduction

Arctic ecosystems are warming rapidly (IPCC, 2013) and plant communities are responding (Elmendorf et al., 2015, 2012b; Myers-Smith et al., 2019, 2011). Yet there is limited understanding of the controls on vegetation change in tundra plant communities. Shrub growth is climate sensitive (Elmendorf et al., 2012a; Myers-Smith et al., 2020) and increases in shrub abundance and decreases in bare ground in plant communities have been reported at sites around the tundra biome (Elmendorf et al., 2012b; Myers-Smith et al., 2011). However, we do not yet have standardized methods of quantifying changes in tundra plant canopy structures and growth across the landscape and there are few allometric relationships relating observable plant dimensions to aboveground biomass in Arctic ecosystems (Berner et al., 2015). One of the key challenges in tundra ecological monitoring is acquiring scale-appropriate observations due to the small growth forms of many plants in this large extent and often less accessible biome (Fisher et al., 2018).

Remote-sensing approaches have been widely employed to gather information about changing Arctic landscapes (Berner et al., 2015; Jia et al., 2009; Myers-Smith et al., 2020; Walker et al., 2003a). In tundra ecosystems, there is a critical scale gap between biome-wide coarse grain observations from satellite-based remote sensing (with pixels typically measuring between 64 km<sup>2</sup> to 625 m<sup>2</sup>) and *in-situ* observations collected at fine spatial scales typically over a few meters (Myers-Smith et al., 2020; Riihimäki et al., 2019; Santin-Janin et al., 2009). Bridging this scale gap requires the integration of observations at intermediate scales. Unmanned aerial vehicles (UAVs, hereafter “drones”) are one possible platform for deploying sensors to collect high-resolution data at landscape scales (Anderson, 2016), and drones are now widely used for collecting environmental data. However, empirical work is needed to relate remotely-sensed attributes to ecological variables and inform scientific interpretations (Räsänen et al., 2019).

Fine-scale measurements of three-dimensional plant structure can inform biomass prediction (Cunliffe et al., 2016; Fraser et al., 2016; Greaves et al., 2017, 2015). Such methods have been demonstrated with ground-based and airborne light detection and ranging (LiDAR) observations in Arctic tundra landscapes (Greaves et al., 2017, 2015), but also with drone photogrammetry surveys leveraging advances in computer vision approaches (Fraser et al., 2019, 2016). However, few studies have tested the correspondence between photogrammetrically determined canopy height and *in situ* measurements, though there can be important differences in the recording of canopy height are using different measurement techniques (Cunliffe et al., 2016; Stewart et al., 2001). Similarly, few studies have tested the correspondence between photogrammetrically determined canopy height and plant biomass for Arctic plants. Such testing is necessary to inform the successful integration of drone surveys into existing ecological monitoring programmes.

Spectral reflectance measurements from optical remote sensing have long been used to determine vegetation indices (Jia et al., 2003; Myers-Smith et al., 2020; Walker et al., 2003a). The most common index used to monitor vegetation is the normalized difference vegetation index (NDVI), which contrasts the reflectance in the red portion of the spectrum that is maximally absorbed by chlorophyll with the near-infrared (NIR) portion that is highly reflected by leaf and canopy structures (Buchhorn et al., 2016). Several studies have shown that NDVI can be good predictor of photosynthetic tissue biomass (here after phytomass) in Arctic ecosystems (Boelman et al., 2003; Walker et al., 2003a), and NDVI has often also been considered a predictor of total aboveground biomass (Berner et al., 2018; Myers-Smith et al., 2020). However, different plant tissues have different reflectance properties (Bratsch et al., 2017; Räsänen et al., 2019), and aboveground biomass is dominated by non-photosynthetic tissues, such as woody stems, in many communities such as shrublands (Epstein et al., 2012). Logistical challenges have limited the number of empirical studies that have been able to test the relationship between NDVI and *total* aboveground biomass (Berner et al., 2018; although see Boelman et al., 2003; Goswami et al., 2015). Furthermore, there is commonly a scale

miss-match between the extents sampled for spectral reflectance (i.e. the ground sampling distance of a remotely-sensed pixel) and over which aboveground biomass is quantified (Berner et al., 2018; Karlsen et al., 2018). The capacity of peak NDVI to explain variation in total biomass needs further evaluation given the widespread consideration of NDVI as a predictor of total aboveground biomass, combined with the increasing accessibility of spectral reflectance data at ever-finer spatial resolutions (Berner et al., 2018; Fraser et al., 2017; Riihimäki et al., 2019).

In this study, we addressed these tundra biomass monitoring priorities by conducting spatially explicit comparisons between ground-based and drone-based measurements of canopy height, NDVI, and biomass. We worked across a *Salix richardsonii* to graminoid ecotone on a shrub-dominated alluvial fan at a focal tundra research site on Qikiqtaruk-Herschel Island. We examined whether drone data collection combined with image-based modelling approaches yield high-fidelity measurements of vegetation attributes. We tested (i) the correspondence between canopy height models derived from aerial photogrammetry and *in-situ* point framing methods, (ii) how well canopy height predicts aboveground biomass, and (iii) how well peak NDVI values obtained at different spatial grains correspond to observations of total biomass, photosynthetic biomass and leaf biomass. Our analyses test the extent to which drone-based methods can be used to monitor vegetation canopies to infer tundra biomass and productivity.

## 2. Methods

### 2.1. Site description

We conducted our study on Qikiqtaruk - Herschel Island in the Canadian Arctic. Tundra vegetation communities here range from graminoid- to shrub-dominated and are underlain by organic soils and ice-rich permafrost. This site has undergone marked ecological changes in community composition, increases in canopy height and vegetation abundance, decreases in bare ground, and an advance in leaf emergence and flowering over the 18 years of ecological monitoring to date (Myers-Smith et al., 2019). We established a ca. 2 ha<sup>-1</sup> study site across a graminoid-shrub ecotone at the edge of a wet willow shrub-dominated alluvial fan (69.34°N, 138.53°W) (Figure 1).

To constrain the photogrammetric modelling and locate the point clouds in a coordinate reference system, 26 ground control markers (265 mm x 265 mm) were deployed across the site and geolocated to a relative 3D accuracy of  $\leq 0.015$  m with RTK-GNSS equipment (Leica GS10). Coordinates were relative to a local benchmark, geolocated in absolute terms to  $\pm 0.003$  m in X and Y, and  $\pm 0.008$  m in Z (95% confidence interval), using the AUSPOS web service. The markers were situated to be visible from the air, and a high density of markers facilitated image alignment in the texturally complex scenes. We selected 36 square plots of 50 cm x 50 cm for harvesting in June 2016. Plots contained no standing water during the period of observations. The plots were arranged in twelve blocks of three replicates across the range of canopy heights to enable a detailed assessment of the form of the allometric relationships. The corners of each harvest plot were precisely geolocated using the GNSS. To minimise the GNSS survey staff sinking into the often-soft ground, we used a ca. 25 cm<sup>2</sup> 'foot' on the bottom of the staff to dissipate pressure.

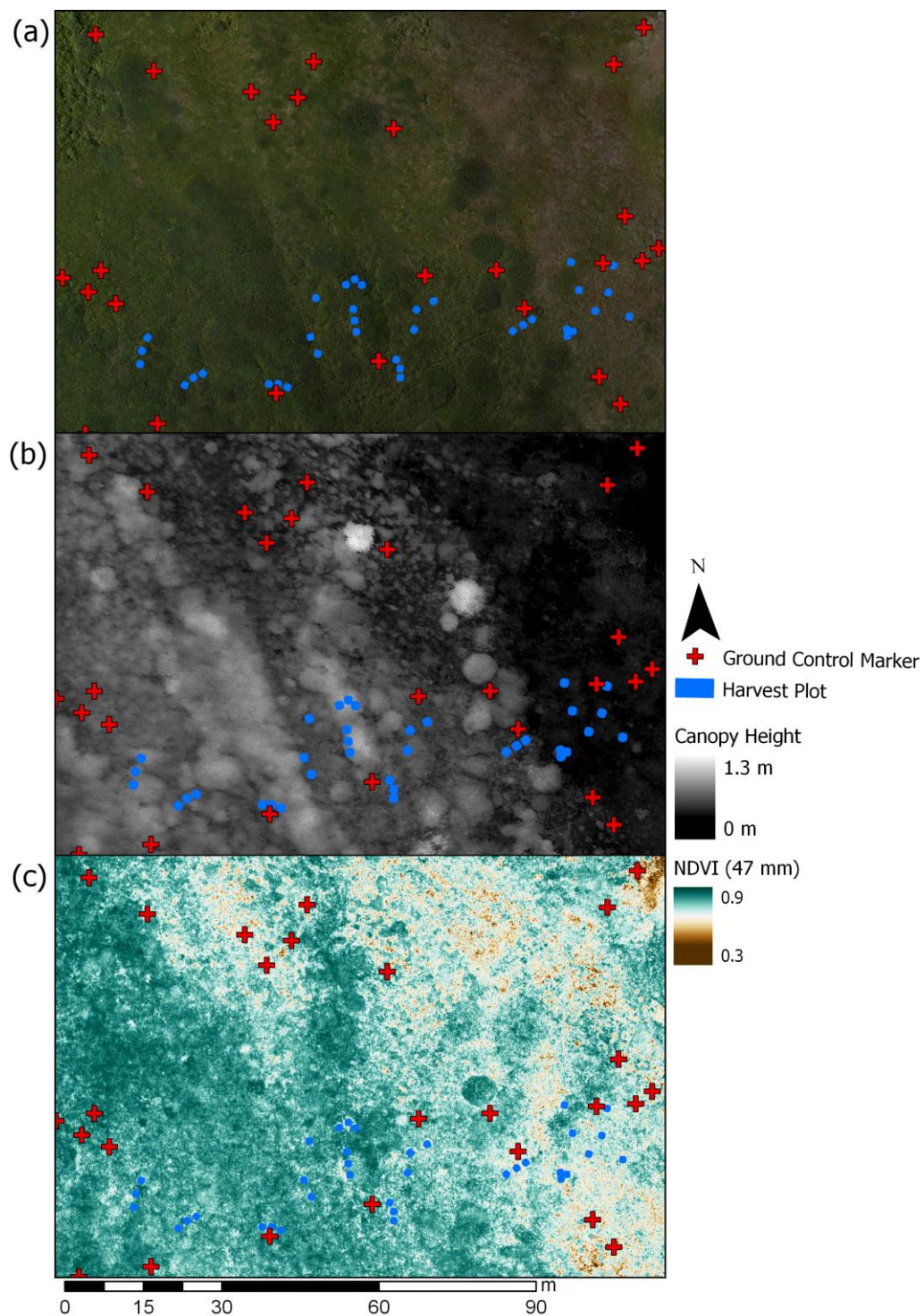


Figure 1. Overview of the study site encompassing a graminoid-shrub ecotone. (a) True colour orthomosaic at 4 mm spatial resolution, (b) structure-from-motion derived canopy height map at 0.01 m spatial grain, and (c) map of NDVI values at 0.047 m spatial grain. The locations of the ground control markers (red crosses, n=26) and harvest plots (blue squares, n=36) are also indicated.

## 2.2. Aerial surveys

### 2.2.1. Aerial survey for canopy height modelling

To obtain aerial images for modelling canopy heights, we used a 24 megapixel camera (Sony α6000), equipped with a prime lens (Sony SEL 20 mm F2.8), carried on a Tarot hexacopter controlled with a PixHawk running open source ArduPilot (<http://ardupilot.org>) software (Table 1). Two sets of survey flights were undertaken, the first obtaining nadir imagery and the second obtaining oblique (ca. 20° from nadir) images with a spatial grain of ca. 4-6 mm at the canopy top (Cunliffe and Anderson, 2019). The camera was triggered by the flight controller based on distance travelled, with both sets of flights together capturing  $\geq 22$  photos for every part of the study area (equivalent to forward overlap of 75% and sidelap of 65% for each flight). We collected 673 RGB photographs over our survey area. Mission flight speeds ensured that motion blur during shutter exposure was less than one third of the ground sampling distance. Image data were originally recorded in lossless RAW format (Sony ARW), and were converted to uncompressed TIFF using Sony's Image Data Converter (v4).

### 2.2.1. Aerial survey for spectral reflectance

To learn more about the consistency of the drone-derived NDVI products under real-world operational conditions, we conducted four multispectral surveys under different spatial grain and illumination conditions, using different survey altitude, sun elevation and cloud conditions (Assmann et al., 2018; Fawcett et al., 2020; Stow et al., 2019). To obtain images for modelling spectral reflectance, we used Parrot Sequoia (Paris, France) multispectral sensors (firmware 1.0.0), mounted on multi-rotor (as above) and flying-wing (Zeta Phantom FX-61) platforms with PixHawk flight controllers. We undertook four multispectral surveys over two days, at altitudes of 19 m, 50 m, 120 m and 121 m above ground level, to sample a range of spatial resolutions and illumination conditions with respect to cloud cover and sun illumination angle (Table 1). The three multirotor flights carried the same Sequoia sensor, while the flying-wing carried a second Sequoia sensor. A MicaSense spectral reflection calibration panel reflecting ca. 50% of light was photographed before and after each survey, and the image considered



to be the most representative of illumination conditions during the survey was used to calibrate the spectral reflectance during processing (Assmann et al., 2018). The reflectance values of the panel were measured under laboratory conditions before and after the field campaign, and we used the mean of these two measurements to minimise errors arising from degradation in panel reflectance. The Sequoia was triggered using a two-second intervalometer to achieve an overlap of at least five images across the area of interest. Our sampling at the end of July coincided with the peak growing season at this location.

Table 1. Description of drone surveys. (A) and (B) refer to the two Parrot Sequoia sensors, and local time refers to the middle of the survey period.

| Sensor             | Altitude<br>agl [m] | GSD<br>[m] | Date                       | Local<br>time<br>(UTC-8) | Solar<br>elevation<br>(degrees) | Platform    | Mean<br>wind<br>speed<br>[m s <sup>-1</sup> ] | Cloud conditions                     |
|--------------------|---------------------|------------|----------------------------|--------------------------|---------------------------------|-------------|---|--------------------------------------|
| Sony α6000         | 19                  | 0.005      | 25 <sup>th</sup> July 2016 | 13:20                    | 39.9                            | Multirotor  | 3.4   | Thin cirrus (sun not obscured)       |
| Parrot Sequoia (A) | 19                  | 0.018      | 26 <sup>th</sup> July 2016 | 17:34                    | 27.3                            | Multirotor  | 3.1   | Thin cirrus (sun not obscured)       |
| Parrot Sequoia (A) | 50                  | 0.047      | 30 <sup>th</sup> July 2016 | 13:10                    | 38.7                            | Multirotor  | 4.2   | Scattered cumulus (sun not obscured) |
| Parrot Sequoia (B) | 120                 | 0.119      | 30 <sup>th</sup> July 2016 | 13:21                    | 38.7                            | Flying wing | 4.9   | Cumulus (sun obscured)               |
| Parrot Sequoia (A) | 121                 | 0.121      | 26 <sup>th</sup> July 2016 | 19:50                    | 15.6                            | Multirotor  | 3.1   | Scattered cumulus (sun not obscured) |

## 2.3. Image based modelling

### 2.3.1. Processing for canopy height models

The aerial images were processed using structure-from-motion photogrammetry on a high performance workstation with a workflow based on Cunliffe *et al.* (2016). Geotagged image data and marker coordinates were imported into Agisoft PhotoScan (v1.2.4) and converted into a common coordinate reference system (WGS84 UTM 7N; EPSG:32607). Image sharpness was assessed using PhotoScan's image quality tool, which assesses the sharpness of the sharpest part of each photograph; all images had a sharpness of  $\geq 0.77$ . Photos were matched and cameras aligned, using the highest quality setting, key point limit of 100,000; unlimited tie points, generic and reference pair preselection enabled, and adaptive camera model fitting disabled. Camera location accuracy was set to 25 m, marker location

accuracy was set to 0.01 m, marker projection accuracy was set to 2 pixels, and tie point accuracy was set to 1.

The sparse cloud was filtered and tie points with reprojection error above 0.55 were excluded from further analysis. An operator reviewed the estimated camera positions to verify their plausibility and remove any obviously erroneous tie points from the sparse cloud. Geolocated markers were manually placed on all projected images for each of the 26 ground control points (Cunliffe et al., 2016; Kachamba et al., 2016). Three markers used for independent accuracy assessment were deselected at this stage. The bundle adjustment was then optimised using the filtered cloud of tie points and the following lens parameters: Focal length ( $f$ ), principal point ( $c_x$ ,  $c_y$ ), radial distortion ( $k_1$ ,  $k_2$ ,  $k_3$ ), tangential distortion ( $p_1$ ,  $p_2$ ), and aspect ratio and skew coefficients ( $b_1$ ,  $b_2$ ). Out of 673 images, 95% (636) were aligned and used for the multi-view stereopsis (dense cloud generation) using the ultrahigh quality setting, mild depth filtering and point colour calculation enabled. The dense point cloud was exported in the .laz format, with point coordinate and RGB attributes.

The dense point cloud was analysed in PDAL (v1.9.1 PDAL Contributors, 2019). The corner coordinates were used to subset points for each harvest plot. Within each plot, the normalised height above ground (hereafter height) of each point was calculated relative to the horizontally closest corner coordinate. Any points with a negative height above ground were coerced to zero. In a few instances where corner marker posts were visible in the point cloud, these points were removed manually. We determined the maximum height for each cell across a fine grid with a spatial resolution of 0.01 m using the rasterstats package (v0.13.1). For cells containing no points, maximum heights were interpolated with inverse distance weighting considering an array of 11 x 11 cells using a power term of two, and cells with no neighbouring points in that area remained empty. We used the 1 cm spatial grain to preserve the fine-scale variability in the point cloud (Cunliffe et al., 2016; Wallace et al., 2017). Plot-level summary metrics were then extracted from this grid of local maxima elevations.

### 2.3.2. Processing for spectral reflectance

The multispectral images were processed using Pix4Dmapper Pro (v4.0.25). We implemented radiometric corrections using downwelling sun irradiance and pre- or post-flight images of reflectance panels following Assmann *et al.* (2018). Ground control markers were manually placed in  $\geq 15$  images, and then automatic placement was employed and manually verified. Normalised difference vegetation index (NDVI) maps were generated using the 'AG Multispectral Template' at the native resolution of the GSD (Table 1). The R Package 'exactextractr' (Baston, 2019, v0.1.1) was used to extract the mean NDVI of each plot, using aerial weighting to avoid the edge effects associated with inclusion or exclusion of boundary pixels.

### 2.4. In-situ point framing

Each of the 36 50 x 50 cm plots were surveyed using point-intercept methodologies similar to ITEX protocols (Molau and Mølgaard, 1996; Myers-Smith *et al.*, 2019), on the 30<sup>th</sup> and 31<sup>st</sup> of July 2016. We placed a grid with 36 points at 10 cm intervals over each plot. At each point, we placed a metal pin vertically and recorded the maximum height of the canopy above the moss/litter layer, as a pseudo-ground surface.

### 2.5. Biomass harvest

Within each of the 36 sub-plots, all standing vascular plants were harvested down to the top of the moss/litter layer (after Walker *et al.*, 2003a) on the 31<sup>st</sup> of July and 1<sup>st</sup> of August 2016. Harvested biomass was separated into three partitions: (i) woody stems, (ii) shrub leaves (including catkins that accounted for less than 10% of the 'leaf' biomass), and (iii) herbaceous material (consisting of mainly graminoids and equisetum flowers, leaves and stems, but also some forbs). Biomass was dried at ca. 35°C for  $\geq 70$  hours, until it reached a constant weight ( $<0.2\%$  change) over a 24-hour period. To quantify biomass carbon contents, subsamples of each partition from 12 plots were oven-dried at 70°C for 48 hours, homogenised for a fine

powder with a ball mill, and flash combusted for measurement of evolved CO<sub>2</sub> in an elemental analyser (CE Instruments, NC2500) at the University of Edinburgh.

## 2.6. Statistical analysis

Statistical analysis was conducted in R (v3.6.1) (R Core Team, 2019). Solar elevations were calculated using the 'suncalc' package (v0.5.0) (Thieurmél and Elmarhraoui, 2019). To compare agreement between point framing and structure-from-motion metrics of canopy height, we calculated concordance correlation coefficients using the 'DescTools' package (after Lin, 1989) and we described this relationship with a power function fitted with ordinary least squares regression because using a positive exponent means the model passes through the origin. We used least squares optimisation to fit linear models between canopy height and aboveground biomass, with intercepts constrained through the origin as plants with zero height above ground have no biomass above ground. Constraining model intercepts made only small differences to model slopes (Table S1). We reported errors as standard deviations unless otherwise stated. We used least squares optimisation to fit exponential models between NDVI and three biomass pools: (i) total aboveground biomass, (ii) phytomass (calculated as the sum of shrub leaves and herbaceous material), and (iii) the biomass of shrub leaves. Comparisons between remotely-sensed NDVI and biomass usually have a substantial mismatch in observation extents due to the larger grain of satellite optical products relative to smaller extents of directly measured harvest plots (Berner et al., 2018), but we undertook spatially explicit drone-based sampling of corresponding areas, so thus our biomass and NDVI measurements do not have this scale mismatch. Because non-harvested moss can contribute to the differential reflectance of red and near-infrared energy, we hypothesized that the proportion of moss cover might influence the relationships between NDVI and biomass. We extracted the proportion of moss cover from our point framing observations and tested the influence of moss cover on NDVI-biomass relationships by adding an interaction term in our model of the relationship between NDVI and phytomass.

### 3. Results

#### 3.1. Drone photogrammetry captured variation in plant canopy height

We found strong agreement between canopy heights as observed with point framing techniques and structure-from-motion photogrammetry (Figures 2 and S1). The photogrammetrically derived canopy heights had a consistent positive bias relative to point framing heights, with a median difference of  $0.14 \pm 0.05$  m ( $\pm$  SD). Differences in mean canopy height between methods were smaller for the shortest and tallest plots, and greatest for the plots of intermediate heights (Figure S1). The concordance correlation coefficient was 0.79 (with 95% confidence intervals of 0.68 to 0.86).

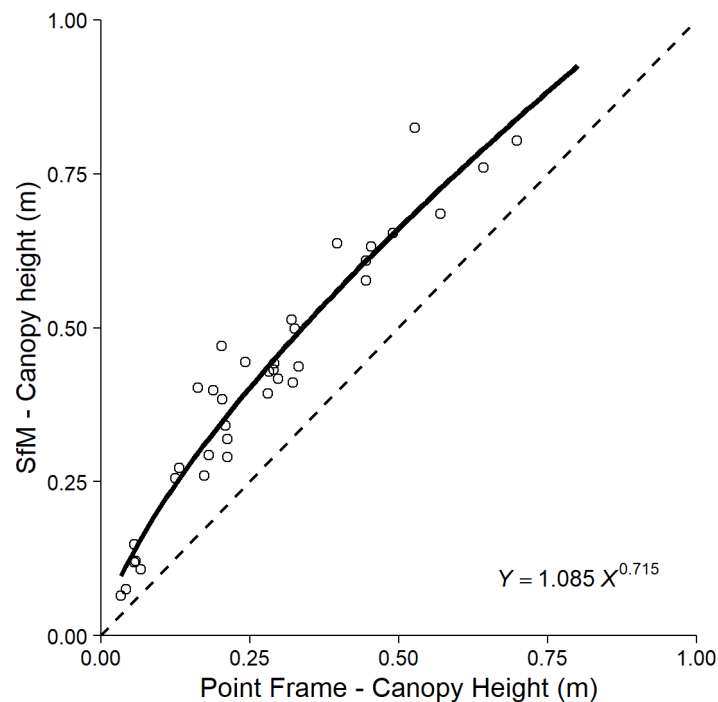


Figure 2. Canopy heights observed with point framing were positively correlated with canopy heights observed with structure-from-motion photogrammetry (SfM). Open circles represent observed values. The dotted line shows the 1:1 relationship for reference and the solid line is a power model. Canopy heights measured with SfM were consistently positively biased, on average by 0.14 m, relative to canopy heights measured with point framing.

### 3.2. Canopy height explained variation in total biomass across plots

We found canopy height explained most of the variation in aboveground biomass across the *Salix richardsonii*-dominated graminoid-shrub ecotone. The models had slopes of  $3623 \pm 177 \text{ g m}^{-1}$  and  $2522 \pm 143 \text{ g m}^{-1}$ , explaining 0.92 and 0.90 of the variance for point intercept and SfM-derived canopy heights respectively (Figure 3). Total aboveground biomass within the sampled plots ranged from  $149 \text{ g m}^2$  to  $2,431 \text{ g m}^2$  with a mean of  $1012 \pm 699 \text{ g m}^2$ . Shrubs (woody material and leaves) accounted for the majority of biomass in 32 of the 36 plots. The biomass of shrub leaves was positively related to total biomass (slope =  $19 \text{ g m}^{-2}$ ), and the biomass of shrub leaves explains 70% of the variation in total biomass (Figure 5a). However, phytomass, calculated as the sum of shrub leaves and herbaceous material, did not correspond with total biomass (Figure 5b). Herbaceous material (largely equisetum and some forbs) typically accounted for half of the phytomass in each harvest plot, ranging from 3% to 87% of the phytomass.

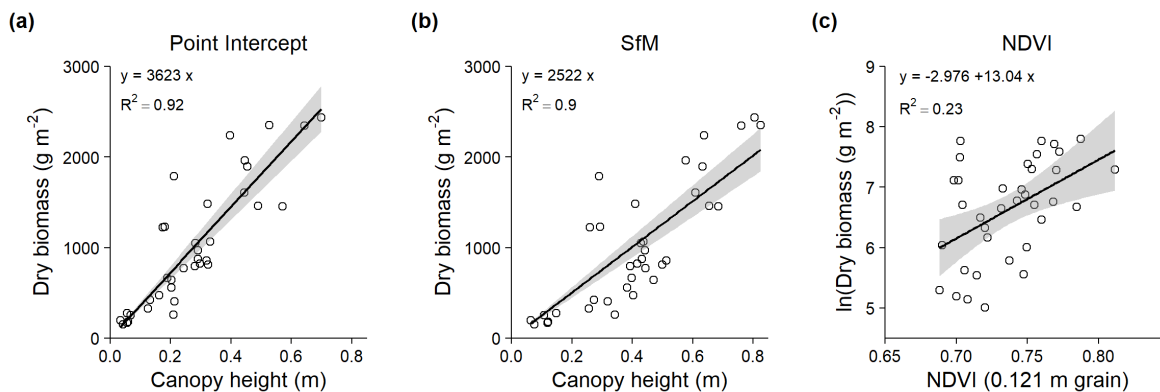
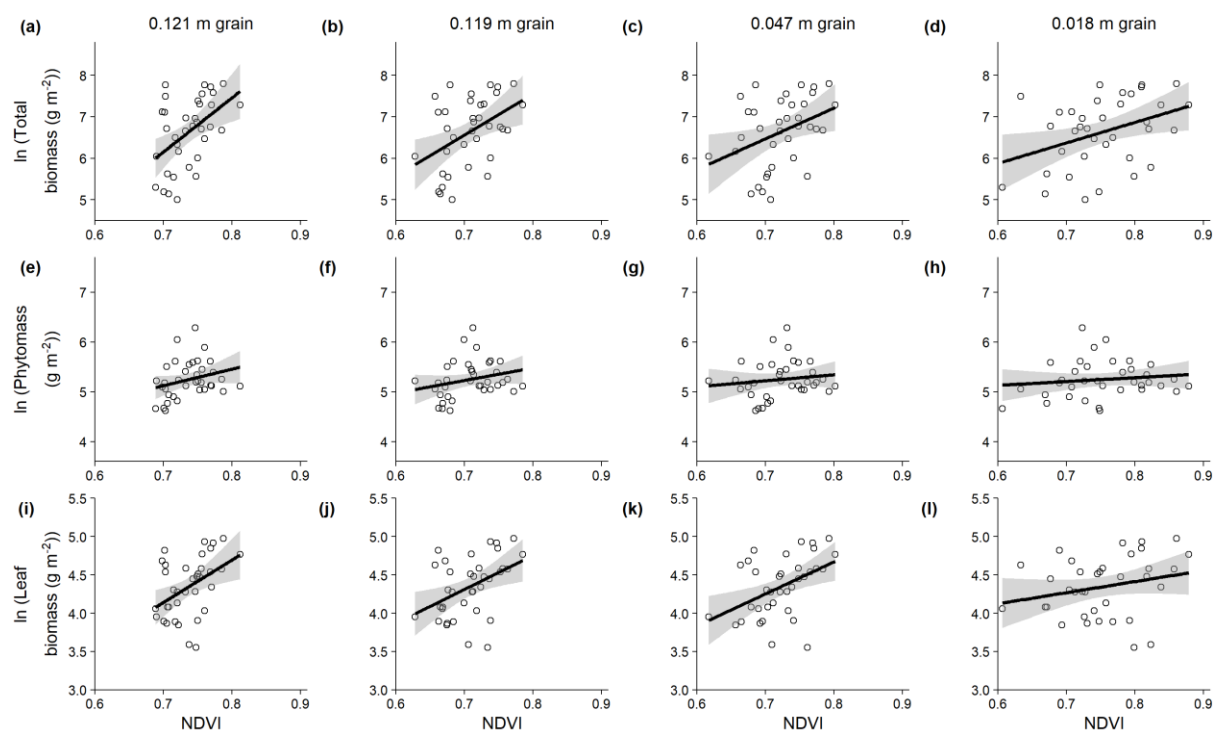


Figure 3. Aboveground biomass was strongly predicted by canopy height but less strongly by NDVI. For each harvest plot, the mean canopy height was measured with (a) point intercept and (b) structure-from-motion photogrammetry, and (c) mean NDVI was extracted from the 0.121 m grain raster. Linear models with constrained intercepts were fitted using least mean squares optimisation, with constrained intercepts for the canopy height models. The linear model fit is a simplification of the likely saturating relationships that we would expect across the full variation of NDVI and biomass values.

### 3.3. NDVI weakly explained biomass

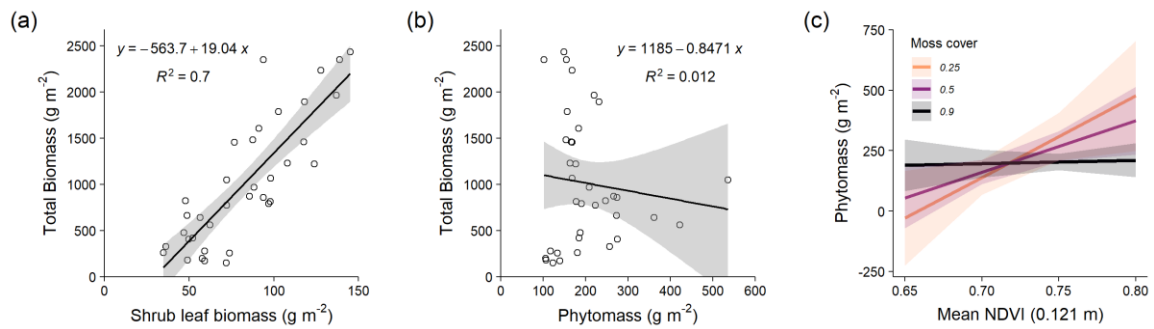
We found that NDVI was positively related to total aboveground biomass, phytomass or shrub leaf biomass (Figures 3c, 4 and S3, Tables 2 and S2). However, NDVI explained just 14% to 23%, 2% to 7% and 6% to 21% of the variance in total aboveground biomass, phytomass and leaf biomass across all four spatial grains investigated (Figure 4, Table 2). Phytomass was calculated as the sum of shrub leaves and herbaceous material, and leaf biomass typically accounted for less than 10% of total biomass. The predictive relationships weakened slightly as the spatial grain of the NDVI rasters became finer from 0.121 m to 0.018 m, with larger residual standard errors and smaller coefficients of determinations (Table 2). As the spatial grain becomes coarser, there is a slight reduction in the overall mean and variability amongst plot NDVI values (Figure S2a). The coarsest spatial grain (0.121 m) appears to deviate slightly from this pattern, and we speculate that this may relate to the more pronounced bi-directional reflectance functions experienced during this survey with a lower sun elevation of just 15.6 degrees (Table 1). The mass of leaf material was a reasonable predictor of total biomass ( $y = -63.7 + 19.04 x$ ;  $R^2 = 0.70$ ; Figure 5a); however, phytomass was a poor predictor of total biomass ( $y = -1185 + 0.8471x$ ;  $R^2 = 0.01$ ; Figure 5b). We tested whether the proportion of moss cover influenced the relationship between NDVI and total biomass, phytomass biomass and the three biomass pools (Table S3, Figure S4), but only found a significant ( $p < 0.05$ ) interaction for the phytomass relationship for the 0.121 m raster (Figure 5c).



349 Figure 4. Mean NDVI is positively but weakly related to total biomass, phytomass and leaf  
350 biomass at the plot level. Open circles represent observations, and black lines are linear  
351 models fitted to the log transformed biomass data, described in Table 2. Exponential models  
352 fitted to non-transformed biomass data are presented in Figure S3 and Table S2.



353



354

355 Figure 5. As shrubs are the dominant species in this landscape, total aboveground biomass  
 356 was predicted strongly by shrub leaf biomass, but not by overall phytomass. (a) The mass of  
 357 shrub leaves explained 70% of the variation in total biomass, but (b) phytomass, calculated  
 358 as the sum of shrub leaves and herbaceous material, explained none of the variation in total  
 359 biomass. (c) The proportion of moss cover only had a significant influence on the relationship  
 360 between NDVI and phytomass for the 0.121 m grain raster. The relationship between NDVI  
 361 and phytomass is strong when moss cover was low but weakens as moss cover increases  
 362 (See Figure S4 for non-significant interactions for other biomass pools and NDVI products).

363 Table 2. Parameters of linear models fitted to mean plot normalised difference vegetation  
 364 index (NDVI) and log transformed total aboveground biomass, phytomass (leaf + herbaceous),  
 365 and leaf biomass (n = 36 in all cases).

| Dependent variable | grain of NDVI in m | Model form        | a                 | b                  | R <sup>2</sup> | Residual standard error |
|--------------------|--------------------|-------------------|-------------------|--------------------|----------------|-------------------------|
| Total biomass      | 0.121              | $\ln(Y) = aX + b$ | $13.04 \pm 4.049$ | $-2.976 \pm 2.987$ | 0.23           | 0.737                   |
| Total biomass      | 0.119              | $\ln(Y) = aX + b$ | $9.902 \pm 3.373$ | $-0.372 \pm 2.39$  | 0.20           | 0.752                   |
| Total biomass      | 0.047              | $\ln(Y) = aX + b$ | $7.412 \pm 3.103$ | $1.282 \pm 2.244$  | 0.14           | 0.779                   |
| Total biomass      | 0.018              | $\ln(Y) = aX + b$ | $4.947 \pm 2.037$ | $2.909 \pm 1.539$  | 0.15           | 0.777                   |
| Phytomass          | 0.121              | $\ln(Y) = aX + b$ | $3.307 \pm 2.005$ | $2.808 \pm 1.479$  | 0.07           | 0.365                   |
| Phytomass          | 0.119              | $\ln(Y) = aX + b$ | $2.518 \pm 1.646$ | $3.464 \pm 1.166$  | 0.06           | 0.367                   |
| Phytomass          | 0.047              | $\ln(Y) = aX + b$ | $1.207 \pm 1.496$ | $4.374 \pm 1.082$  | 0.02           | 0.376                   |
| Phytomass          | 0.018              | $\ln(Y) = aX + b$ | $0.772 \pm 0.985$ | $4.664 \pm 0.744$  | 0.02           | 0.376                   |
| Leaf biomass       | 0.121              | $\ln(Y) = aX + b$ | $5.54 \pm 1.937$  | $0.263 \pm 1.428$  | 0.19           | 0.353                   |
| Leaf biomass       | 0.119              | $\ln(Y) = aX + b$ | $4.429 \pm 1.589$ | $1.213 \pm 1.126$  | 0.19           | 0.354                   |
| Leaf biomass       | 0.047              | $\ln(Y) = aX + b$ | $4.183 \pm 1.389$ | $1.326 \pm 1.005$  | 0.21           | 0.349                   |
| Leaf biomass       | 0.018              | $\ln(Y) = aX + b$ | $1.45 \pm 0.998$  | $3.255 \pm 0.754$  | 0.06           | 0.381                   |

366 Where  $\pm$  refers to the standard error of the parameter and n = 36 in all cases.

#### 4. Discussion

We found that canopy heights across a graminoid-shrub ecotone could be measured over fine (cm) spatial scales using structure-from-motion photogrammetry. Heights derived from drone photogrammetry corresponded strongly with those obtained from using conventional point intercept techniques (Molau and Mølgaard, 1996; Myers-Smith et al., 2019). Canopy heights were positively correlated with biomass, indicating that photogrammetry-derived data can be used to estimate aboveground tundra biomass. However, vegetation greenness as measured by NDVI only weakly corresponded with biomass observations and was influenced by the amount of moss cover on the ground. Our findings suggest that the relationship between fine-grain peak NDVI and biomass can be influenced by other types of evergreen vegetation cover. Our study highlights that drone-derived canopy height and biomass estimates could help inform monitoring of vegetation change and improve projections of plant responses to warming in tundra ecosystems.

##### *Photogrammetry-derived canopy heights were taller than in situ measured canopy heights*

We attribute the positive bias in canopy heights measured with point intercept relative to photogrammetry to differences in the way the two approaches quantify canopy architecture. Similar good correspondence between *in-situ* versus photogrammetrically-derived *maximum* canopy heights has also been reported for 20 shrubs measured at an Arctic tundra site near Cambridge Bay (Clement and Fraser, 2017). However, such comparisons are hindered by the sensitivity of maximum height measurements to outliers in these often noisy point clouds (Cunliffe et al., 2016). The photogrammetry-derived heights in our study may have also been slightly exaggerated by slight depression of the moss 'ground' surface (ca. 2 - 3 cm) at the plot corners by the survey staff. Photogrammetrically-derived canopy heights are sensitive to the ways in which raw data are acquired, processed and analysed (Cunliffe et al., 2016; Fraser et al., 2019; Wallace et al., 2017). Our findings suggest that, when applied in a consistent manner, drone photogrammetry is an appropriate tool for monitoring shrub canopy heights in such ecosystems.

395

396 *Canopy heights predict aboveground biomass*

397 Our finding that canopy height strongly predicted aboveground biomass for this *Salix*  
398 *richardsonii* community corroborates similar reports for photogrammetry across a range of  
399 biomes and plant communities (Bendig et al., 2015; Grüner et al., 2019; Selsam et al., 2017;  
400 Wijesingha et al., 2018). Estimating aboveground biomass from canopy height models  
401 depends on having an underlying terrain model of sufficient quality to describe topographic  
402 variability (Cunliffe et al., 2016; Fraser et al., 2019). In this study, we derived our terrain model  
403 using RTK-GNSS observations of plot corners, which can be a viable option for characterising  
404 topography over extents of up to a few hectares. In ecosystems where canopies are spatially  
405 or temporally discontinuous, terrain models could also be derived directly from  
406 photogrammetric point clouds (Cunliffe et al., 2016; Fraser et al., 2019). Terrain models  
407 derived using other survey techniques could also be co-registered in a hybrid approach  
408 (Dandois and Ellis, 2013). However, propagation of uncertainties including co-registration  
409 error is vital for understanding the limits of detection of genuine change in canopy height  
410 (James et al., 2017).

411

412 *Refining predictions of biomass from canopy height*

413 Relationships between plant dimensions and biomass are sensitive to the ways in which these  
414 measurements are obtained (Cunliffe et al., 2020). Cross-site data syntheses therefore require  
415 the use of standardised protocols for data collection and processing (such as HiLDEN  
416 (<https://arcticdrones.org/>), Assmann et al., 2018; Cunliffe and Anderson, 2019). There is a  
417 need for further coordinated work to calibrate the relationship between photogrammetric-  
418 inferred canopy height and aboveground biomass for different taxonomic groups (Pätzig et al.,  
419 2020). There is also a need to quantify the sensitivity of these relationships to key parameters  
420 (e.g. the spatial resolution of the input data, the implementation of multi-view stereopsis and  
421 the spatial grain of analysis, sensu Wallace et al., 2017; Zarco-Tejada et al., 2014), as well as

to differences in environmental conditions (e.g. illumination conditions and wind-induced movement of plant canopies, sensu Dandois et al., 2015).

#### *Vegetation greenness only weakly corresponds with biomass*

We found that NDVI only weakly predicted aboveground biomass at this site, explaining at most 23% of the variation in total biomass, and even less of the variance in phytomass or leaf biomass (Figures 4 and S3, Tables 2 and S2). Inferring aboveground biomass from NDVI is predicated on the assumptions that (i) NDVI is a good predictor of phytomass, and (ii) that phytomass is a good predictor of total biomass. We found that while NDVI had some capacity to explain variance in phytomass (Figure 4, Table 2), phytomass was a very weak predictor of total biomass (Figure 5b). Across spatial grains, predictive relationships weakened slightly as the spatial grain of the NDVI rasters became finer from 0.121 m to 0.018 m (Table 2). We attribute two main causes for the weak correspondence between the vegetation index and biomass. Firstly, although leaf biomass was a strong predictor of total aboveground biomass, leaf biomass accounted for typically only half of the phytomass in each plot, and phytomass (including herbaceous material and shrub leaves) was poorly related to total biomass (Figure 5). Consequently, vegetation indices that integrate all photosynthetically active material might be a poor predictor of total biomass (Bratsch et al., 2017; Räsänen et al., 2019). Secondly, we found indications of an influence of moss cover on the relationship between NDVI and phytomass. This interaction effect was only significant in one of the 12 combinations of NDVI raster and biomass pool tested, but was consistent in the direction of the effect indicating that the NDVI-phytomass relationship was mediated by the amount of moss cover beneath the sampled vegetation and weakened as moss cover increased (Figures 5C and S4).

The low correspondence between NDVI and phytomass that we observed contrasts with reports of stronger positive relationships between NDVI and aboveground biomass derived from datasets compiled across different spatial scales (Boelman et al., 2003; Goswami et al., 2015; Walker et al., 2003b). NDVI has a saturating relationship with biomass and NDVI-

biomass relationships can be confounded by a variety of ecological variables, land-surface properties and view angle effects (Buchhorn et al., 2016; Karlsen et al., 2018; Myers-Smith et al., 2020; Walker et al., 2003a). Our findings are consistent with the well-known saturation effect in this spectrum of NDVI values (e.g., Berner et al., 2018). Our results highlight a need for caution when total biomass maps are derived from vegetation indices products in high latitude ecosystems with variable land cover, particularly at finer spatial grains. The biome-wide tundra greening patterns and trends observed with large-grain satellite datasets are unlikely to directly represent plant functional attributes such as canopy height or biomass *in situ* (Myers-Smith et al., 2020). Thus, to improve our understanding of vegetation greening in tundra ecosystems across vegetation types and geographic gradients, we need data collection across scales from focal sites to the tundra biome (Fisher et al., 2018; Miller et al., 2019; Myers-Smith et al., 2020).

## **5. Conclusion**

This study expands the empirical understanding of how fine-grained remotely-sensed observations relate to vegetation attributes. By comparing structural, spectral reflectance and on-the-ground ecological metrics, we can improve our understanding of scaling relationships from fine- to coarse-scale observations of tundra vegetation change. Drone-collected data are already helping us to fill in the missing landscape scale gap in tundra ecological monitoring, and future work needs to continue using coordinated protocols to underpin biome-scale data synthesis (e.g. HiLDEN (<https://arcticdrones.org/>) and Cunliffe and Anderson, 2019). We found strong agreement in canopy heights measured using *in-situ* point framing compared to drone-photogrammetry. Canopy height was strongly and linearly related to aboveground biomass, explaining ca. 90% of the observed variability in the biomass. Vegetation 'greenness' measured as NDVI across four independent multispectral surveys explained only a small proportion of the variability in total biomass and was influenced by moss cover, suggesting caution should be used when attributing differences in NDVI to differences in either biomass or phytomass. Our comparison of structural, spectral and *in-situ* ecological measurements

478 contributes to improved understanding of tundra vegetation as inferred from remote sensing  
479 and informs projections tundra vegetation change with warming.  
480

## **Statement of contribution**

A.M.C and I.H.M.-S. conceived the research idea. A.M.C., J.A. and I.H.M.-S. developed the experimental design. I.H.M.-S. acquired the funding. A.M.C., J.A., J.K. and I.H.M.-S. undertook the investigation. A.M.C. and G.D. completed the analysis. A.M.C. led the writing of the manuscript and data visualisation. All authors contributed to the final version of the manuscript.

## **Data accessibility**

The data reported here, including dry sample weights, drone-acquired photographs, coordinates of harvest plots and ground control markers and the derived dense point cloud are available through the NERC Polar Data Centre (DOI: **XXX TO BE CONFIRMED**). The code for statistical analyses and data visualisation is available from <https://github.com/AndrewCunliffe/OrcaManuscript>.

## **Conflicts of interest**

The authors declare no conflicts of interest.

## **Acknowledgements**

This work was supported by NERC ShrubTundra project (NE/M016323/1), and the loan of GNSS equipment from NERC GEF (NERC/GEF: 1063 and 1069). The authors wish to thank the Inuvialuit people for permission to work on their traditional lands, and the Yukon Government and Parks for their permission and logistical support for this research (Permit number Inu-02-16). We thank the Herschel Island – Qikiqtaruk Territorial Park rangers for logistical support of this research. Drone flight operations were authorised by a Special Flight Operations Certificate granted by Transport Canada. We thank Haydn Thomas, Sandra Angers-Blondin, Eleanor Walker, John Godlee and Santeri Lehtonen for assistance with fieldwork.



509 **References**

- 510 Anderson, K., 2016. Integrating multiple scales of remote sensing measurement – from  
 511 satellites to kites. *Prog. Phys. Geogr.* 40, 187–195.  
 512 <https://doi.org/10.1177/0309133316639175>
- 513 Assmann, J.J., Kerby, J.T., Cunliffe, A.M., Myers-Smith, I.H., 2018. Vegetation monitoring  
 514 using multispectral sensors - best practices and lessons learned from high latitudes.  
 515 *J. Unmanned Veh. Syst.* 334730. <https://doi.org/10.1101/334730>
- 516 Baston, D., 2019. exactextractr. ISciences, LLC.
- 517 Bendig, J., Yu, K., Aasen, H., Bolten, A., Bennertz, S., Broscheit, J., Gnyp, M.L., Bareth, G.,  
 518 2015. Combining UAV-based plant height from crop surface models, visible, and near  
 519 infrared vegetation indices for biomass monitoring in barley. *Int. J. Appl. Earth Obs.*  
 520 *Geoinformation* 39, 79–87. <https://doi.org/10.1016/j.jag.2015.02.012>
- 521 Berner, L.T., Alexander, H.D., Loranty, M.M., Ganzlin, P., Michelle, M.C., Davydov, S.P.,  
 522 Goetz, S.J., 2015. Biomass allometry for alder, dwarf birch, and willow in boreal forest  
 523 and tundra ecosystems of far northeastern Siberia and north-central Alaska. *For. Ecol.*  
 524 *Manag.* 337, 110–118. <https://doi.org/10.1016/j.foreco.2014.10.027>
- 525 Berner, L.T., Jantz, P., Tape, K.D., Goetz, S.J., 2018. Tundra plant above-ground biomass  
 526 and shrub dominance mapped across the North Slope of Alaska. *Environ. Res. Lett.*  
 527 13, 035002. <https://doi.org/10.1088/1748-9326/aaaa9a>
- 528 Boelman, N.T., Stieglitz, M., Rueth, H.M., Sommerkorn, M., Griffin, K.L., Shaver, G.R.,  
 529 Gamon, J.A., 2003. Response of NDVI, biomass, and ecosystem gas exchange to  
 530 long-term warming and fertilization in wet sedge tundra. *Oecologia* 135, 414–421.  
 531 <https://doi.org/10.1007/s00442-003-1198-3>
- 532 Bratsch, S., Epstein, H., Buchhorn, M., Walker, D., Landes, H., 2017. Relationships between  
 533 hyperspectral data and components of vegetation biomass in Low Arctic tundra  
 534 communities at Ivotuk, Alaska. *Environ. Res. Lett.* 12, 025003.  
 535 <https://doi.org/10.1088/1748-9326/aa572e>
- 536 Buchhorn, M., Reynolds, M.K., Walker, D.A., 2016. Influence of BRDF on NDVI and biomass  
 537 estimations of Alaska Arctic tundra. *Environ. Res. Lett.* 11, 125002.  
 538 <https://doi.org/10.1088/1748-9326/11/12/125002>
- 539 Clement, C., Fraser, R.H., 2017. Shrub monitoring in Canada's Arctic using multi-scale  
 540 measurements from field plots, unmanned aerial vehicles and satellite remote sensing  
 541 (No. POLAR Project PKC-NST-1617-004). Polar Knowledge Canada.
- 542 Cunliffe, A., Anderson, K., 2019. Measuring Above-ground Biomass with Drone  
 543 Photogrammetry: Data Collection Protocol. *Protoc. Exch.*  
 544 <https://doi.org/10.1038/protex.2018.134>
- 545 Cunliffe, A.M., Brazier, R.E., Anderson, K., 2016. Ultra-fine grain landscape-scale  
 546 quantification of dryland vegetation structure with drone-acquired structure-from-  
 547 motion photogrammetry. *Remote Sens. Environ.* 183, 129–143.  
 548 <https://doi.org/10.1016/j.rse.2016.05.019>
- 549 Cunliffe, A.M., McIntire, C.D., Boschetti, F., Sauer, K.J., Litvak, M., Anderson, K., Brazier,  
 550 R.E., 2020. Allometric relationships for predicting aboveground biomass and sapwood  
 551 area of Oneseed Juniper (*Juniperus monosperma*) trees. *Front. Plant Sci.* 11.  
 552 <https://doi.org/10.3389/fpls.2020.00094>
- 553 Dandois, J.P., Ellis, E.C., 2013. High spatial resolution three-dimensional mapping of  
 554 vegetation spectral dynamics using computer vision. *Remote Sens. Environ.* 136, 259–  
 555 276. <https://doi.org/10.1016/j.rse.2013.04.005>
- 556 Dandois, J.P., Olano, M., Ellis, E.C., 2015. Optimal altitude, overlap, and weather conditions  
 557 for computer vision UAV estimates of forest structure. *Remote Sens.* 7, 13895–13920.  
 558 <https://doi.org/10.3390/rs71013895>
- 559 Elmendorf, S.C., Henry, G.H.R., Hollister, R.D., Björk, R.G., Boulanger-Lapointe, N., Cooper,  
 560 E.J., Cornelissen, J.H.C., Day, T.A., Dorrepaal, E., Elumeeva, T.G., Gill, M., Gould,  
 561 W.A., Harte, J., Hik, D.S., Hofgaard, A., Johnson, D.R., Johnstone, J.F., Jónsdóttir,  
 562 I.S., Jorgenson, J.C., Klanderud, K., Klein, J.A., Koh, S., Kudo, G., Lara, M., Lévesque,

- E., Magnússon, B., May, J.L., Mercado-Díaz, J.A., Michelsen, A., Molau, U., Myers-Smith, I.H., Oberbauer, S.F., Onipchenko, V.G., Rixen, C., Martin Schmidt, N., Shaver, G.R., Spasojevic, M.J., Þórhallsdóttir, Þ.E., Tolvanen, A., Troxler, T., Tweedie, C.E., Villareal, S., Wahren, C.-H., Walker, X., Webber, P.J., Welker, J.M., Wipf, S., 2012a. Plot-scale evidence of tundra vegetation change and links to recent summer warming. *Nat. Clim. Change* 2, 453–457. <https://doi.org/10.1038/nclimate1465>
- Elmendorf, S.C., Henry, G.H.R., Hollister, R.D., Björk, R.G., Boulanger-Lapointe, N., Cooper, E.J., Cornelissen, J.H.C., Day, T.A., Dorrepaal, E., Elumeeva, T.G., Gill, M., Gould, W.A., Harte, J., Hik, D.S., Hofgaard, A., Johnson, D.R., Johnstone, J.F., Jónsdóttir, I.S., Jorgenson, J.C., Klanderud, K., Klein, J.A., Koh, S., Kudo, G., Lara, M., Lévesque, E., Magnússon, B., May, J.L., Mercado-Díaz, J.A., Michelsen, A., Molau, U., Myers-Smith, I.H., Oberbauer, S.F., Onipchenko, V.G., Rixen, C., Schmidt, N.M., Shaver, G.R., Spasojevic, M.J., Þórhallsdóttir, Þ.E., Tolvanen, A., Troxler, T., Tweedie, C.E., Villareal, S., Wahren, C.-H., Walker, X., Webber, P.J., Welker, J.M., Wipf, S., 2012b. Plot-scale evidence of tundra vegetation change and links to recent summer warming. *Nat. Clim. Change* 2, 453–457. <https://doi.org/10.1038/nclimate1465>
- Elmendorf, S.C., Henry, G.H.R., Hollister, R.D., Fosaa, A.M., Gould, W.A., Hermanutz, L., Hofgaard, A., Jónsdóttir, I.I., Jorgenson, J.C., Lévesque, E., Magnusson, B., Molau, U., Myers-Smith, I.H., Oberbauer, S.F., Rixen, C., Tweedie, C.E., Walker, M., 2015. Experiment, monitoring, and gradient methods used to infer climate change effects on plant communities yield consistent patterns. *Proc. Natl. Acad. Sci.* 112, 448–452. <https://doi.org/10.1073/pnas.1410088112>
- Epstein, H.E., Raynolds, M.K., Walker, D.A., Bhatt, U.S., Tucker, C.J., Pinzon, J.E., 2012. Dynamics of aboveground phytomass of the circumpolar Arctic tundra during the past three decades. *Environ. Res. Lett.* 7, 015506. <https://doi.org/10.1088/1748-9326/7/1/015506>
- Fawcett, D., Panigada, C., Tagliabue, G., Boschetti, M., Celesti, M., Evdokimov, A., Biriukova, K., Colombo, R., Miglietta, F., Rascher, U., Anderson, K., 2020. Multi-scale evaluation of drone-based multispectral surface reflectance and vegetation indices in operational conditions. *Remote Sens.* 12, 514. <https://doi.org/10.3390/rs12030514>
- Fisher, J.B., Hayes, D.J., Schwalm, C.R., Huntzinger, D.N., Stofferahn, E., Schaefer, K., Luo, Y., Wulschleger, S.D., Goetz, S., Miller, C.E., Griffith, P., Chadburn, S., Chatterjee, A., Ciais, P., Douglas, T.A., Genet, H., Ito, A., Neigh, C.S.R., Poulter, B., Rogers, B.M., Sonnentag, O., Tian, H., Wang, W., Xue, Y., Yang, Z.-L., Zeng, N., Zhang, Z., 2018. Missing pieces to modeling the Arctic-Boreal puzzle. *Environ. Res. Lett.* 13, 020202. <https://doi.org/10.1088/1748-9326/aa9d9a>
- Fraser, R.H., Lantz, T.C., McFarlane-Winchester, M., van der Sluijs, J., Prevost, C., 2019. Testing the potential of UAV photogrammetry for deriving bare earth models in arctic shrublands (No. XXXXX). Geomatics Canada.
- Fraser, R.H., Olthof, I., Lantz, T.C., Schmitt, C., 2016. UAV photogrammetry for mapping vegetation in the low-Arctic. *Arct. Sci.* 2, 79–102. <https://doi.org/10.1139/as-2016-0008>
- Fraser, R.H., van der Sluijs, J., Hall, R.J., 2017. Calibrating satellite-based indices of burn severity from UAV-derived metrics of a burned boreal forest in NWT, Canada. *Remote Sens.* 9, 279. <https://doi.org/10.3390/rs9030279>
- Goswami, S., Gamon, J., Vargas, S., Tweedie, C., 2015. Relationships of NDVI, Biomass, and Leaf Area Index (LAI) for six key plant species in Barrow, Alaska. *PeerJ.* [https://doi.org/DOI: 10.7287/peerj.preprints.913v1](https://doi.org/DOI:10.7287/peerj.preprints.913v1)
- Greaves, H.E., Vierling, L.A., Eitel, J.U.H., Boelman, N.T., Magney, T.S., Prager, C.M., Griffin, K.L., 2017. Applying terrestrial lidar for evaluation and calibration of airborne lidar-derived shrub biomass estimates in Arctic tundra. *Remote Sens. Lett.* 8, 175–184. <https://doi.org/10.1080/2150704X.2016.1246770>
- Greaves, H.E., Vierling, L.A., Eitel, J.U.H., Boelman, N.T., Magney, T.S., Prager, C.M., Griffin, K.L., 2015. Estimating aboveground biomass and leaf area of low-stature Arctic shrubs with terrestrial LiDAR. *Remote Sens. Environ.* 164, 26–35. <https://doi.org/10.1016/j.rse.2015.02.023>

- Grüner, E., Astor, T., Wachendorf, M., 2019. Biomass prediction of heterogeneous temperate grasslands using an SfM approach based on UAV imaging. *Agronomy* 9, 54. <https://doi.org/10.3390/agronomy9020054>
- IPCC, 2013. Climate Change 2013: The Physical Science Basis. Contribution of Working Group I to the Fifth Assessment Report of the Intergovernmental Panel on Climate Change, in: Stocker, T.F., Qin, D., Plattner, G.-K., Tignor, M.M.B., Allen, S.K., Boschung, J., Nauels, A., Xia, Y., Bex, V., Midgley, P. (Eds.), . Cambridge University Press, Cambridge, United Kingdom, p. 996.
- James, M.R., Robson, S., Smith, M.W., 2017. 3-D uncertainty-based topographic change detection with structure-from-motion photogrammetry: precision maps for ground control and directly georeferenced surveys. *Earth Surf. Process. Landf.* 42, 1769–1788. <https://doi.org/10.1002/esp.4125>
- Jia, G.J., Epstein, H.E., Walker, D.A., 2009. Vegetation greening in the Canadian Arctic related to decadal warming. *J. Environ. Monit.* 11, 2231–2238. <https://doi.org/10.1039/B911677J>
- Jia, G.J., Epstein, H.E., Walker, D.A., 2003. Greening of Arctic Alaska, 1981–2001. *Geophys. Res. Lett.* 30, 2067. <https://doi.org/10.1029/2003GL018268>
- Kachamba, D.J., Ørka, H.O., Gobakken, T., Eid, T., Mwase, W., 2016. Biomass estimation using 3D data from unmanned aerial vehicle imagery in a tropical woodland. *Remote Sens.* 8, 968. <https://doi.org/10.3390/rs8110968>
- Karlsen, S.R., Anderson, H.B., Wal, R. van der, Hansen, B.B., 2018. A new NDVI measure that overcomes data sparsity in cloud-covered regions predicts annual variation in ground-based estimates of high arctic plant productivity. *Environ. Res. Lett.* 13, 025011. <https://doi.org/10.1088/1748-9326/aa9f75>
- Lin, L.I.-K., 1989. A concordance correlation coefficient to evaluate reproducibility. *Biometrics* 45, 255–268. <https://doi.org/10.2307/2532051>
- Miller, C.E., Griffith, P.C., Goetz, S.J., Hoy, E.E., Pinto, N., McCubbin, I.B., Thorpe, A.K., Hofton, M., Hodkinson, D., Hansen, C., Woods, J., Larson, E., Kasischke, E.S., Margolis, H.A., 2019. An overview of ABoVE airborne campaign data acquisitions and science opportunities. *Environ. Res. Lett.* 14, 080201. <https://doi.org/10.1088/1748-9326/ab0d44>
- Molau, U., Mølgaard, P., 1996. ITEX Manual.
- Myers-Smith, I.H., Forbes, B.C., Wilmking, M., Hallinger, M., Lantz, T., Blok, D., Tape, K.D., Macias-Fauria, M., Sass-Klaassen, U., Lévesque, E., Boudreau, S., Ropars, P., Hermanutz, L., Trant, A.J., Collier, L.S., Weijers, S., Rozema, J., Rayback, S.A., Schmidt, N.M., Schaepman-Strub, G., Wipf, S., Rixen, C., Ménard, C.B., Venn, S., Goetz, S., Andreu-Hayles, L., Elmendorf, S., Ravolainen, V., Welker, J., Grogan, P., Epstein, H.E., Hik, D.S., 2011. Shrub expansion in tundra ecosystems: dynamics, impacts and research priorities. *Environ. Res. Lett.* 6, 045509. <https://doi.org/10.1088/1748-9326/6/4/045509>
- Myers-Smith, I.H., Grabowski, M., Thomas, H.J.D., Angers-Blondin, S., Daskalova, G., Bjorkman, A.D., Cunliffe, A.M., Assmann, J., Boyle, J., McLeod, E., McLeod, S., Joe, R., Lennie, P., Arey, D., Gordon, R., Eckert, C., 2019. Eighteen years of ecological monitoring reveals multiple lines of evidence for tundra vegetation change. *Ecol. Monogr.* 89. <https://doi.org/10.1002/ecm.1351>
- Myers-Smith, I.H., Kerby, J.T., Phoenix, G.K., Bjerke, J.W., Epstein, H.E., Assmann, J.J., John, C., Andreu-Hayles, L., Angers-Blondin, S., Beck, P.S.A., Berner, L.T., Bhatt, U.S., Bjorkman, A.D., Blok, D., Bryn, A., Christiansen, C.T., Cornelissen, J.H.C., Cunliffe, A.M., Elmendorf, S.C., Forbes, B.C., Goetz, S.J., Hollister, R.D., Jong, R. de, Loranty, M.M., Macias-Fauria, M., Maseyk, K., Normand, S., Olofsson, J., Parker, T.C., Parmentier, F.-J.W., Post, E., Schaepman-Strub, G., Stordal, F., Sullivan, P.F., Thomas, H.J.D., Tømmervik, H., Treharne, R., Tweedie, C.E., Walker, D.A., Wilmking, M., Wipf, S., 2020. Complexity revealed in the greening of the Arctic. *Nat. Clim. Change* 10, 106–117. <https://doi.org/10.1038/s41558-019-0688-1>

- Pätzig, M., Geiger, F., Rasche, D., Rauneker, P., Eltner, A., 2020. Allometric relationships for selected macrophytes of kettle holes in northeast Germany as a basis for efficient biomass estimation using unmanned aerial systems (UAS). *Aquat. Bot.* 162, 103202. <https://doi.org/10.1016/j.aquabot.2020.103202>
- PDAL Contributors, 2019. PDAL Point Data Abstraction Library.
- R Core Team, 2019. R: A language and environment for statistical computing. R Foundation for Statistical Computing, Vienna, Austria.
- Räsänen, A., Juutinen, S., Aurela, M., Virtanen, T., 2019. Predicting aboveground biomass in Arctic landscapes using very high spatial resolution satellite imagery and field sampling. *Int. J. Remote Sens.* 40, 1175–1199. <https://doi.org/10.1080/01431161.2018.1524176>
- Riihimäki, H., Luoto, M., Heiskanen, J., 2019. Estimating fractional cover of tundra vegetation at multiple scales using unmanned aerial systems and optical satellite data. *Remote Sens. Environ.* 224, 119–132. <https://doi.org/10.1016/j.rse.2019.01.030>
- Santin-Janin, H., Garel, M., Chapuis, J.-L., Pontier, D., 2009. Assessing the performance of NDVI as a proxy for plant biomass using non-linear models: a case study on the Kerguelen archipelago. *Polar Biol.* 32, 861–871. <https://doi.org/10.1007/s00300-009-0586-5>
- Selsam, P., Schaeper, W., Brinkmann, K., Buerkert, A., 2017. Acquisition and automated rectification of high-resolution RGB and near-IR aerial photographs to estimate plant biomass and surface topography in arid agro-ecosystems. *Exp. Agric.* 53, 144–157. <https://doi.org/10.1017/S0014479716000089>
- Stewart, K.E.J., Bourn, N. a. D., Thomas, J.A., 2001. An evaluation of three quick methods commonly used to assess sward height in ecology. *J. Appl. Ecol.* 38, 1148–1154. <https://doi.org/10.1046/j.1365-2664.2001.00658.x>
- Stow, D., Nichol, C.J., Wade, T., Assmann, J.J., Simpson, G., Helfter, C., 2019. Illumination geometry and flying height influence surface reflectance and NDVI derived from ultispectral UAS imagery. *Drones* 3, 55. <https://doi.org/10.3390/drones3030055>
- Thieurmél, B., Elmarhraoui, A., 2019. Package ‘suncalc.’
- Walker, D.A., Epstein, H.E., Jia, G.J., Balser, A., Copass, C., Edwards, E.J., Gould, W.A., Hollingsworth, J., Knudson, J., Maier, H.A., Moody, A., Raynolds, M.K., 2003a. Phytomass, LAI, and NDVI in northern Alaska: Relationships to summer warmth, soil pH, plant functional types, and extrapolation to the circumpolar Arctic. *J. Geophys. Res. Atmospheres* 108, 8169. <https://doi.org/10.1029/2001JD000986>
- Walker, D.A., Epstein, H.E., Jia, G.J., Balser, A., Copass, C., Edwards, E.J., Gould, W.A., Hollingsworth, J., Knudson, J., Maier, H.A., Moody, A., Raynolds, M.K., 2003b. Phytomass, LAI, and NDVI in northern Alaska: Relationships to summer warmth, soil pH, plant functional types, and extrapolation to the circumpolar Arctic. *J. Geophys. Res. Atmospheres* 108, 8169. <https://doi.org/10.1029/2001JD000986>
- Wallace, L., Hillman, S., Reinke, K., Hally, B., 2017. Non-destructive estimation of above-ground surface and near-surface biomass using 3D terrestrial remote sensing techniques. *Methods Ecol. Evol.* 8, 1607–1616. <https://doi.org/10.1111/2041-210X.12759>
- Wijesingha, J., Moeckel, T., Hensgen, F., Wachendorf, M., 2018. Evaluation of 3D point cloud-based models for the prediction of grassland biomass. *Int. J. Appl. Earth Obs. Geoinformation.* <https://doi.org/10.1016/j.jag.2018.10.006>
- Zarco-Tejada, P.J., Diaz-Varela, R., Angileri, V., Loudjani, P., 2014. Tree height quantification using very high resolution imagery acquired from an unmanned aerial vehicle (UAV) and automatic 3D photo-reconstruction methods. *Eur. J. Agron.* 55, 89–99. <https://doi.org/10.1016/j.eja.2014.01.004>

### **Supplementary Information**

Table S1. Models describing the relationships between height and aboveground biomass. Using mean canopy heights, where SfM is structure-from-motion,  $\pm$  is model standard error and  $n = 36$  in all cases.

| Canopy height method | Model form                       | Intercept          | Slope              | R <sup>2</sup> | P       |
|----------------------|----------------------------------|--------------------|--------------------|----------------|---------|
| Point Framing        | AGB = Height x Slope + Intercept | 31.5 $\pm$ 112.2   | 3539.8 $\pm$ 345.8 | 0.76           | <0.0001 |
| Point Framing        | AGB = Height x Slope             |                    | 3622.8 $\pm$ 177.7 | 0.92           | <0.0001 |
| SfM                  | AGB = Height x Slope + Intercept | -174.8 $\pm$ 150.2 | 2864.3 $\pm$ 326.4 | 0.69           | <0.0001 |
| SfM                  | AGB = Height x Slope             |                    | 2522.3 $\pm$ 142.7 | 0.90           | <0.0001 |

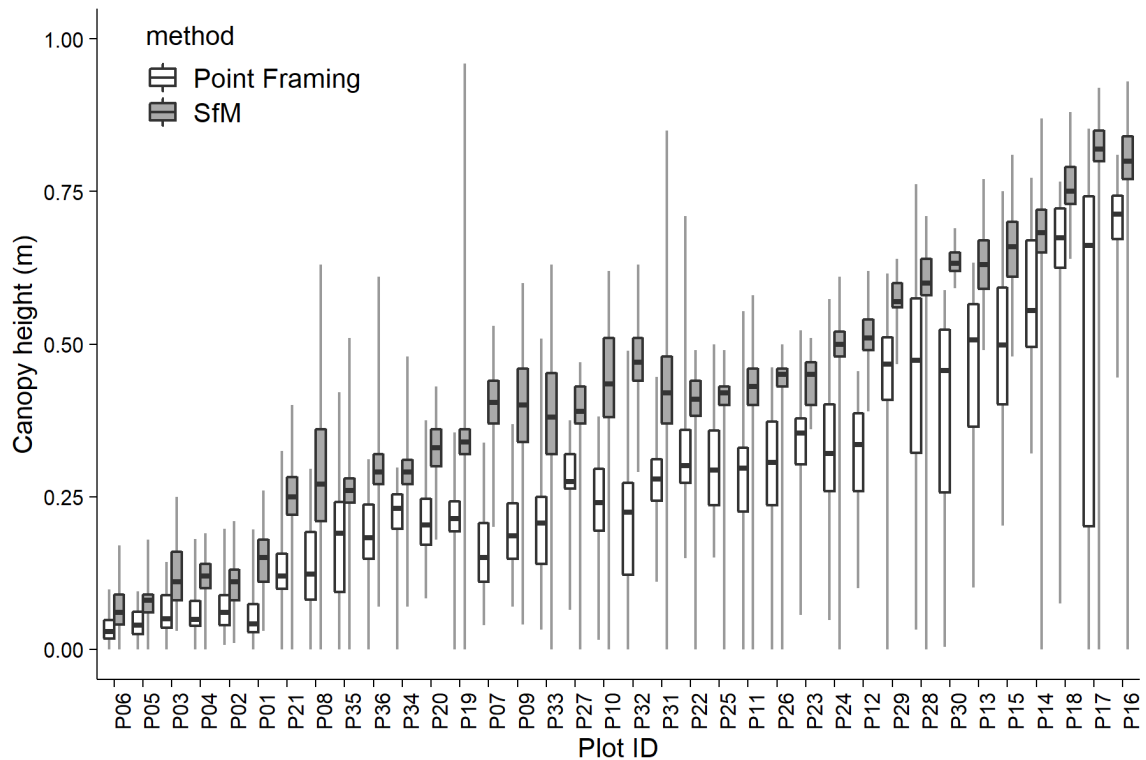
729 Table S2. Parameters of exponential models fitted to mean plot normalised difference  
730 vegetation index (NDVI) and total aboveground biomass, phytomass (leaf + herbaceous), and  
731 leaf biomass. Where  $\pm$  refers to the standard error of the parameter and  $n = 36$  in all cases.

| Dependent variable | grain of NDVI in<br>m | Model form              | a                 | b                     | Residual<br>standard<br>error |
|--------------------|-----------------------|-------------------------|-------------------|-----------------------|-------------------------------|
| Total biomass      | 0.121                 | $Y = a e^{(b \cdot X)}$ | $9.475 \pm 3.221$ | $0.901 \pm 2.194$     | 634.328                       |
| Total biomass      | 0.119                 | $Y = a e^{(b \cdot X)}$ | $7.29 \pm 2.89$   | $5.616 \pm 11.816$    | 648.573                       |
| Total biomass      | 0.047                 | $Y = a e^{(b \cdot X)}$ | $6.743 \pm 2.724$ | $7.459 \pm 15.135$    | 652.475                       |
| Total biomass      | 0.018                 | $Y = a e^{(b \cdot X)}$ | $4.061 \pm 1.744$ | $46.041 \pm 63.156$   | 656.433                       |
| Phytomass          | 0.121                 | $Y = a e^{(b \cdot X)}$ | $2.247 \pm 2.365$ | $38.918 \pm 68.261$   | 89.504                        |
| Phytomass          | 0.119                 | $Y = a e^{(b \cdot X)}$ | $1.77 \pm 1.963$  | $58.286 \pm 81.611$   | 89.639                        |
| Phytomass          | 0.047                 | $Y = a e^{(b \cdot X)}$ | $0.877 \pm 1.777$ | $108.331 \pm 139.843$ | 90.51                         |
| Phytomass          | 0.018                 | $Y = a e^{(b \cdot X)}$ | $0.288 \pm 1.167$ | $164.353 \pm 145.315$ | 90.775                        |
| Leaf biomass       | 0.121                 | $Y = a e^{(b \cdot X)}$ | $5.974 \pm 1.717$ | $0.996 \pm 1.281$     | 26.979                        |
| Leaf biomass       | 0.119                 | $Y = a e^{(b \cdot X)}$ | $4.924 \pm 1.471$ | $2.494 \pm 2.648$     | 27.124                        |
| Leaf biomass       | 0.047                 | $Y = a e^{(b \cdot X)}$ | $4.694 \pm 1.338$ | $2.736 \pm 2.704$     | 26.703                        |
| Leaf biomass       | 0.018                 | $Y = a e^{(b \cdot X)}$ | $1.954 \pm 0.941$ | $18.845 \pm 13.673$   | 29.365                        |

732

Table S3. Model parameters predicting biomass (total biomass, phytomass (leaf + herbaceous), and leaf biomass) as a function of normalised difference vegetation index (NDVI) and the proportion of moss cover ('moss') including an interaction between NDVI and moss cover ( n = 36 in all cases).

| Dependent variable | NDVI Grain (m) | Term      | Estimate | Standard error | Statistic | P value |
|--------------------|----------------|-----------|----------|----------------|-----------|---------|
| Total              | 0.121          | Intercept | -746.69  | 10733.47       | -0.07     | 0.945   |
| Total              | 0.121          | NDVI      | 2199.21  | 14916.16       | 0.147     | 0.884   |
| Total              | 0.121          | moss      | -6964.96 | 12976.43       | -0.537    | 0.595   |
| Total              | 0.121          | NDVI:moss | 9657.19  | 17964.49       | 0.538     | 0.595   |
| Total              | 0.119          | Intercept | -1020.71 | 6271.7         | -0.163    | 0.872   |
| Total              | 0.119          | NDVI      | 2709.27  | 9145           | 0.296     | 0.769   |
| Total              | 0.119          | moss      | -4147.05 | 7743.37        | -0.536    | 0.596   |
| Total              | 0.119          | NDVI:moss | 6043.21  | 11202.14       | 0.539     | 0.593   |
| Total              | 0.047          | Intercept | -350.82  | 5489.47        | -0.064    | 0.949   |
| Total              | 0.047          | NDVI      | 1687.7   | 7920.88        | 0.213     | 0.833   |
| Total              | 0.047          | moss      | -3911.73 | 6725.02        | -0.582    | 0.565   |
| Total              | 0.047          | NDVI:moss | 5645.66  | 9620.09        | 0.587     | 0.561   |
| Total              | 0.018          | Intercept | 3458.56  | 5140.38        | 0.673     | 0.506   |
| Total              | 0.018          | NDVI      | -3802.48 | 7487.36        | -0.508    | 0.615   |
| Total              | 0.018          | moss      | -7446.94 | 6227.87        | -1.196    | 0.241   |
| Total              | 0.018          | NDVI:moss | 10448.67 | 8951.65        | 1.167     | 0.252   |
| Phytomass          | 0.121          | Intercept | -3117.03 | 1412.93        | -2.206    | 0.035   |
| Phytomass          | 0.121          | NDVI      | 4620.53  | 1963.53        | 2.353     | 0.025   |
| Phytomass          | 0.121          | moss      | 3574.6   | 1708.19        | 2.093     | 0.044   |
| Phytomass          | 0.121          | NDVI:moss | -4980.47 | 2364.81        | -2.106    | 0.043   |
| Phytomass          | 0.119          | Intercept | -1347.45 | 833.81         | -1.616    | 0.116   |
| Phytomass          | 0.119          | NDVI      | 2268.22  | 1215.81        | 1.866     | 0.071   |
| Phytomass          | 0.119          | moss      | 1587.83  | 1029.47        | 1.542     | 0.133   |
| Phytomass          | 0.119          | NDVI:moss | -2331.1  | 1489.3         | -1.565    | 0.127   |
| Phytomass          | 0.047          | Intercept | -898.08  | 736.37         | -1.22     | 0.232   |
| Phytomass          | 0.047          | NDVI      | 1593.65  | 1062.52        | 1.5       | 0.143   |
| Phytomass          | 0.047          | moss      | 1225.14  | 902.11         | 1.358     | 0.184   |
| Phytomass          | 0.047          | NDVI:moss | -1774.09 | 1290.46        | -1.375    | 0.179   |
| Phytomass          | 0.018          | Intercept | -325.55  | 720.51         | -0.452    | 0.654   |
| Phytomass          | 0.018          | NDVI      | 774.68   | 1049.48        | 0.738     | 0.466   |
| Phytomass          | 0.018          | moss      | 564.03   | 872.94         | 0.646     | 0.523   |
| Phytomass          | 0.018          | NDVI:moss | -831.93  | 1254.72        | -0.663    | 0.512   |
| Leaf biomass       | 0.121          | Intercept | 307.04   | 445.51         | 0.689     | 0.496   |
| Leaf biomass       | 0.121          | NDVI      | -312.93  | 619.12         | -0.505    | 0.617   |
| Leaf biomass       | 0.121          | moss      | -755.98  | 538.6          | -1.404    | 0.17    |
| Leaf biomass       | 0.121          | NDVI:moss | 1031.48  | 745.64         | 1.383     | 0.176   |
| Leaf biomass       | 0.119          | Intercept | 33.52    | 260.05         | 0.129     | 0.898   |
| Leaf biomass       | 0.119          | NDVI      | 70.99    | 379.18         | 0.187     | 0.853   |
| Leaf biomass       | 0.119          | moss      | -324.18  | 321.07         | -1.01     | 0.32    |
| Leaf biomass       | 0.119          | NDVI:moss | 452.3    | 464.48         | 0.974     | 0.337   |
| Leaf biomass       | 0.047          | Intercept | -65.88   | 222.87         | -0.296    | 0.769   |
| Leaf biomass       | 0.047          | NDVI      | 212.66   | 321.58         | 0.661     | 0.513   |
| Leaf biomass       | 0.047          | moss      | -180.94  | 273.03         | -0.663    | 0.512   |
| Leaf biomass       | 0.047          | NDVI:moss | 238.51   | 390.57         | 0.611     | 0.546   |
| Leaf biomass       | 0.018          | Intercept | 138.41   | 230.61         | 0.6       | 0.553   |
| Leaf biomass       | 0.018          | NDVI      | -82.54   | 335.9          | -0.246    | 0.807   |
| Leaf biomass       | 0.018          | moss      | -258.61  | 279.4          | -0.926    | 0.362   |
| Leaf biomass       | 0.018          | NDVI:moss | 348.08   | 401.59         | 0.867     | 0.393   |



738

739 Figure S1. There was good agreement in canopy heights as observed with point framing (PF)

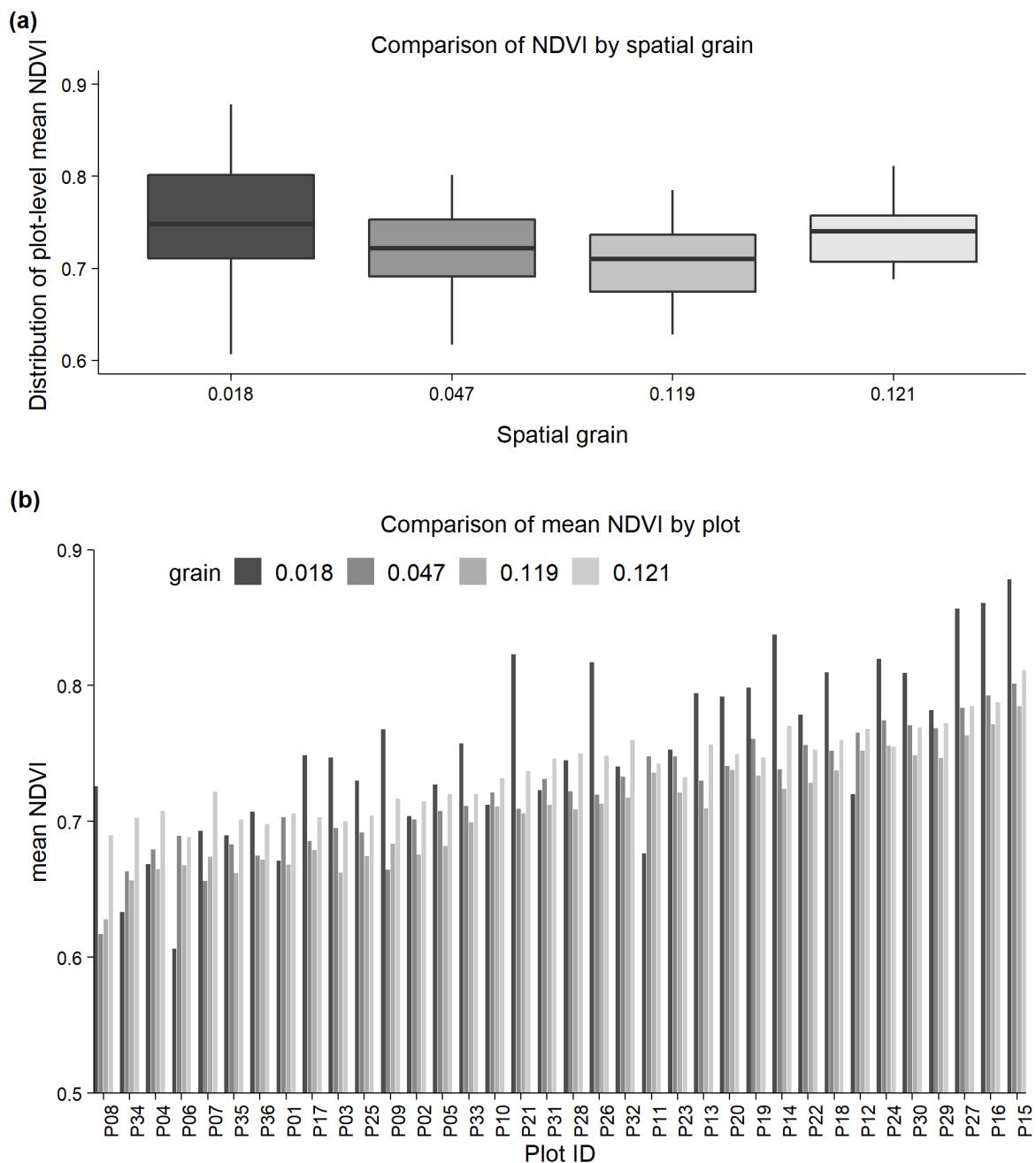
740 and structure-from-motion photogrammetry (SfM) methods. Canopy heights measured with

741 SfM were consistently positively biased relative to canopy heights measured with PF. The

742 central bar indicates median canopy height, the shaded box indicates the interquartile range,

743 and the whiskers indicate the maximum and minimum values.





744

745 Figure S2. (a) Distribution of plot-level mean NDVI values for each spatial grain, and (b) plot-  
 746 wise comparison of mean NDVI from each spatial grain. As the spatial grain becomes coarser,  
 747 there is a slight reduction in NDVI values and a reduction in variability in NDVI values. The  
 748 coarsest spatial grain (0.121 m) appears to deviate slightly from this pattern, and we speculate  
 749 that this may relate to the more pronounced bi-directional reflectance functions experienced  
 750 during this survey with a lower sun elevation of just 15.6 degrees (Table 1).

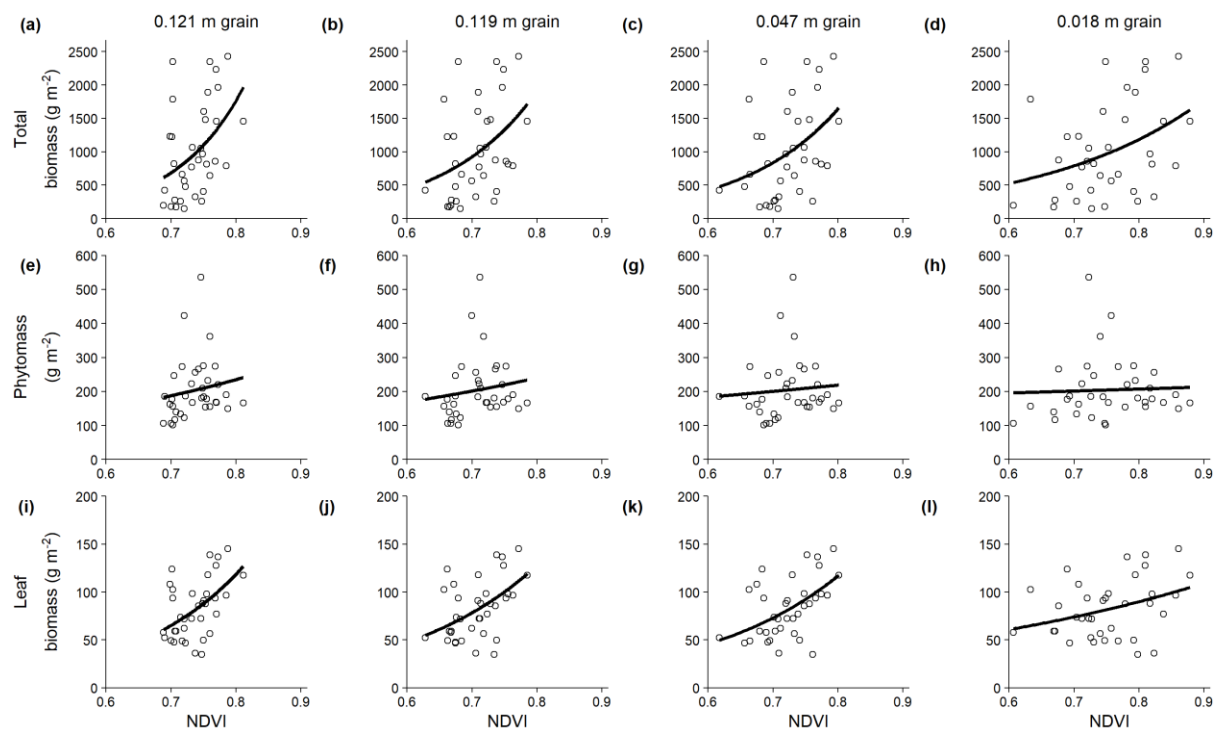
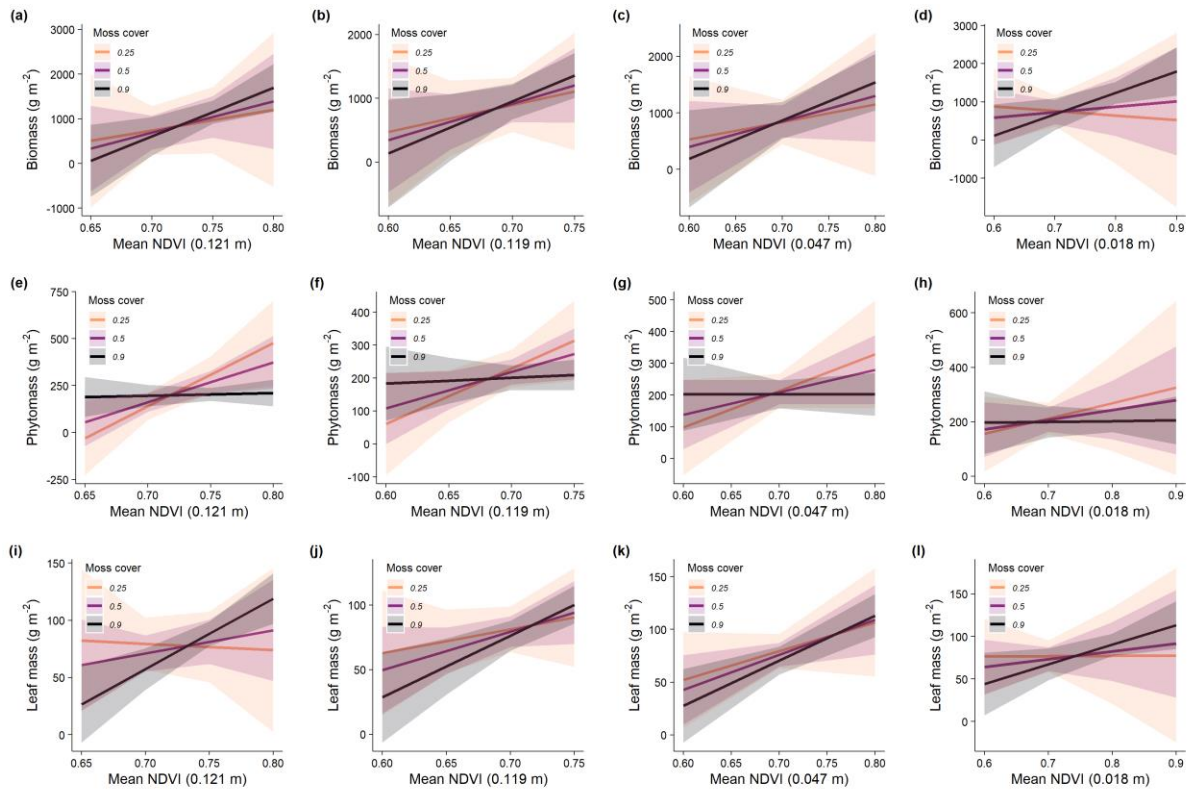


Figure S3. NDVI was positively, but only weakly, related to total biomass, phytomass or leaf biomass at the plot level. Open circles represent observed values, and black lines are exponential models, described in Table S2.



756

757 Figure S4. We tested whether the proportion of moss cover influenced the relationship  
 758 between NDVI and biomass for each biomass pool: total biomass (a, b, c, d), phytomass (e,  
 759 f, g, h) and leaf biomass (i, j, k, l), for each NDVI raster. The interaction was only significant  
 760 ( $p < 0.05$ ) for the phytomass relationship for the 0.121 m raster (panel e), described in Table  
 761 S3.